NASA/TM-2004-212676

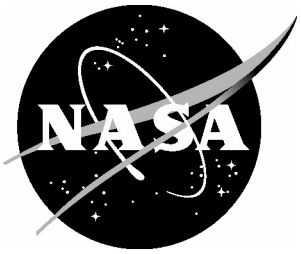

Parametric Study on the Response of Compression-Loaded Composite Shells With Geometric and Material Imperfections

Mark W. Hilburger and James H. Starnes, Jr.
Langley Research Center, Hampton, Virginia

September 2004

The NASA STI Program Office . . . in Profile

Since its founding, NASA has been dedicated to the advancement of aeronautics and space science. The NASA Scientific and Technical Information (STI) Program Office plays a key part in helping NASA maintain this important role.

The NASA STI Program Office is operated by Langley Research Center, the lead center for NASA's scientific and technical information. The NASA STI Program Office provides access to the NASA STI Database, the largest collection of aeronautical and space science STI in the world. The Program Office is also NASA's institutional mechanism for disseminating the results of its research and development activities. These results are published by NASA in the NASA STI Report Series, which includes the following report types:

- TECHNICAL PUBLICATION. Reports of completed research or a major significant phase of research that present the results of NASA programs and include extensive data or theoretical analysis. Includes compilations of significant scientific and technical data and information deemed to be of continuing reference value. NASA counterpart of peer-reviewed formal professional papers, but having less stringent limitations on manuscript length and extent of graphic presentations.

- TECHNICAL MEMORANDUM. Scientific and technical findings that are preliminary or of specialized interest, e.g., quick release reports, working papers, and bibliographies that contain minimal annotation. Does not contain extensive analysis.

- CONTRACTOR REPORT. Scientific and technical findings by NASA-sponsored contractors and grantees.

- CONFERENCE PUBLICATION. Collected papers from scientific and technical conferences, symposia, seminars, or other meetings sponsored or co-sponsored by NASA.

- SPECIAL PUBLICATION. Scientific, technical, or historical information from NASA programs, projects, and missions, often concerned with subjects having substantial public interest.

- TECHNICAL TRANSLATION. English-language translations of foreign scientific and technical material pertinent to NASA's mission.

Specialized services that complement the STI Program Office's diverse offerings include creating custom thesauri, building customized databases, organizing and publishing research results ... even providing videos.

For more information about the NASA STI Program Office, see the following:

- Access the NASA STI Program Home Page at *http://www.sti.nasa.gov*

- E-mail your question via the Internet to help@sti.nasa.gov

- Fax your question to the NASA STI Help Desk at (301) 621-0134

- Phone the NASA STI Help Desk at (301) 621-0390

- Write to:
  NASA STI Help Desk
  NASA Center for AeroSpace Information
  7121 Standard Drive
  Hanover, MD 21076-1320

NASA/TM-2004-212676

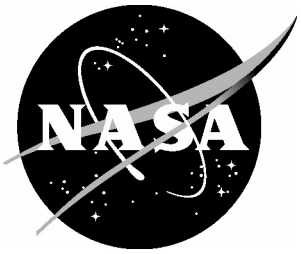

Parametric Study on the Response of Compression-Loaded Composite Shells With Geometric and Material Imperfections

Mark W. Hilburger and James H. Starnes, Jr.
Langley Research Center, Hampton, Virginia

National Aeronautics and
Space Administration

Langley Research Center
Hampton, Virginia 23681-2199

September 2004

Available from:

NASA Center for AeroSpace Information (CASI)
7121 Standard Drive
Hanover, MD 21076-1320
(301) 621-0390
605-6000

National Technical Information Service (NTIS)
5285 Port Royal Road
Springfield, VA 22161-2171
(703)

Abstract

The results of a parametric study of the effects of initial imperfections on the buckling and postbuckling response of three unstiffened thin-walled compression-loaded graphite-epoxy cylindrical shells with different orthotropic and quasi-isotropic shell-wall laminates are presented. The imperfections considered include initial geometric shell-wall midsurface imperfections, shell-wall thickness variations, local shell-wall ply-gaps associated with the fabrication process, shell-end geometric imperfections, nonuniform applied end loads, and variations in the boundary conditions including the effects of elastic boundary conditions. A high-fidelity nonlinear shell analysis procedure that accurately accounts for the effects of these imperfections on the nonlinear responses and buckling loads of the shells is described. The analysis procedure includes a nonlinear static analysis that predicts stable response characteristics of the shells and a nonlinear transient analysis that predicts unstable response characteristics.

Introduction

The increasing need to produce lighter-weight aerospace shell structures has led to the use of advanced material systems in new structural designs, and improved design methods appropriate for these advanced material systems are needed. The high strength-to-weight and high stiffness-to-weight ratios of advanced composite materials offer significant weight reduction potential for aerospace structures. Designers often use a design-level analysis procedure with empirical data to develop new structural designs for strength and buckling critical structures. The traditional approach for designing thin-walled buckling-resistant isotropic shell structures is to predict the buckling load of the shell with a deterministic analysis, and then to reduce this predicted load with an empirical "knockdown" factor (e.g., Ref. 1). The empirical knockdown factor is intended to account for the difference between the predicted buckling load and the actual buckling load for the shell determined from tests. A linear bifurcation buckling analysis is often used for the design-level analysis, and this analysis is usually based on nominal structural dimensions and material properties of an idealized, geometrically perfect shell. The design knockdown factor used in the design of buckling-resistant shells is often based on the "lower bound" design recommendations reported in Reference 1. This design philosophy can result in overly conservative designs for these structures, and it can potentially even result in unconservative designs if the empirical data are not representative of the design of interest. While it is generally recognized that initial geometric shell-wall imperfections are a major contributor to the discrepancy between the predicted shell buckling loads and the experimentally measured shell buckling loads (e.g., Refs. 2-6), the traditional sources of design knockdown factors do not include data or information related to the sensitivity of shell response to various forms of imperfections. In addition, the traditional sources of design knockdown factors for predicting shell buckling loads do not include information for shell structures made from advanced composite materials. Recent studies (e.g., Refs. 7-11) have shown that traditional initial geometric shell-wall imperfections, and other nontraditional forms of imperfections or variations in geometric and material parameters, loading conditions, and boundary conditions can significantly affect the buckling load of a compression-loaded composite shell structure. The effects of these traditional and nontraditional initial imperfections on composite-shell buckling are generally not well understood by structural engineers and designers.

The present paper describes the results of an experimental and analytical study of the effects of traditional initial geometric shell-wall imperfections, and the effects of nontraditional initial imperfections and

variations in other nontraditional geometric and material parameters, loading conditions, and boundary conditions on the buckling response of unstiffened thin-walled compression-loaded graphite-epoxy cylindrical shells. The results of three graphite-epoxy shells with different orthotropic and quasi-isotropic shell-wall laminates are presented, Traditional shell-wall geometric imperfections and several nontraditional imperfections were measured, and representations of these imperfections were included in nonlinear analyses of the shells that were conducted with the geometrically nonlinear STAGS finite element analysis code (Ref. 12). The effects of initial geometric shell-wall imperfections, shell-wall thickness variations, shell-end geometric imperfections, nonuniform applied end loads, and variations in the boundary conditions, including the effects of elastic boundary conditions, on the buckling response of these thin-walled composite shells are discussed in the present paper. The effects of fabrication anomalies caused by small local gaps between adjacent pieces of the graphite-epoxy material in some of the shell-wall laminate plies are also discussed. The results of the study are used to illustrate the significance of these nontraditional initial imperfections on composite shell response characteristics. The nonlinear shell analysis procedure used to predict the nonlinear response and buckling loads of the shells is described, and the analysis results are compared with the experimental results. The use of this nonlinear shell analysis procedure for determining accurate, high-fidelity design knockdown factors for shell buckling and collapse, and for determining the effects of variations and uncertainties in shell geometric and material parameters on shell buckling loads is discussed.

Test Specimens, Imperfection Measurements, and Test Apparatus and Tests

Test Specimens

The specimens tested in this investigation were fabricated from 0.005-in.-thick AS4/3502 graphite-epoxy preimpregnated unidirectional tape material made by Hercules, Inc. The nominal unidirectional lamina properties of a typical 0.005-in.-thick ply with a fiber volume fraction of 0.62 are as follows: longitudinal modulus E_1 = 19.5 Msi, transverse modulus E_2 = 1.45 Msi, in-plane shear modulus G_{12} = 0.813 Msi, and major Poisson's ratio ν_{12} = 0.30. The material was laid up on a mandrel and cured in an autoclave to form three shells with different shell-wall laminates including an axially stiff $[\mp 45/0_2]_s$ laminate, a circumferentially stiff $[\mp 45/90_2]_s$ laminate, and a quasi-isotropic $[\mp 45/0/90]_s$ laminate. The three resulting shells are referred to herein as shells or specimens C1, C2 and C3, respectively. These specimens had a nominal length of 16.0 in., a nominal radius of 8.0 in., and a nominal thickness of 0.04 in. Both ends of the specimens were potted in an aluminum-filled epoxy resin to assure that the ends of the specimens did not fail prematurely during the test. The potting material extended approximately 1.0 inch along the length of the specimens at each end resulting in a test section that was approximately 14.0 in. long. The ends of the specimens were machined flat and parallel to assure proper load introduction during the tests. A photograph of a typical specimen and the specimen coordinate system used to represent the corresponding geometry is shown in Fig.1. The shell length, test-section length, radius, and thickness are designated as L, L_T, R, and t, respectively.

Imperfection Measurements

Three-dimensional surveys of the inner and outer shell-wall surfaces of the specimens were made to determine their initial geometric shell-wall imperfection shapes and shell-wall thickness distributions. Measurements were taken over a uniform grid with increments of 0.125 in. in the axial direction and 0.139 in. (approximately 1^o of arc) in the circumferential direction over the exposed surfaces of the specimens. The inner surface measurement was used to determine the initial geometric shell-wall imperfection shape of a specimen, and the difference between the outer and inner surface measurements was used to determine

the shell-wall thickness distribution. A contour plot of the nondimensionalized initial geometric shell-wall mid-surface imperfections $\overline{w}_o(x,\theta)$ for specimen C3 is shown in Fig. 2. The measured shell-wall imperfection w_o is nondimensionalized by the average measured shell-wall thickness t_{ave} = 0.0381 inches. These results indicate that the initial geometric shell-wall imperfection is periodic in the circumferential direction and has slight deviations in the axial direction. The amplitude of the imperfection varies from $+1.341t_{ave}$ to $-1.535\ t_{ave}$. A contour plot of the nondimensionalized shell-wall thickness variation $\overline{t}_o(x,\theta)$ for specimen C3 is shown in Fig. 3, where the measured thickness value t_o is nondimensionalized by the average measured shell-wall thickness t_{ave}. These results indicate that the shell-wall thickness, and hence the laminate stiffnesses, varies significantly over a short distance. The thickness varies from 0.928 to 1.321 times t_{ave}. Most of the thickness variation is attributed to local variations in the resin content of the laminate associated with the fabrication process. However, the darker angular pattern in the thickness distribution is attributed to small gaps between adjacent pieces of graphite-epoxy tape in some of the laminate plies that were generated during the lay-up and curing processes. Such a region is referred to herein as a lamina ply-gap or a ply-gap. In such a locally thin region, the shell wall consists of a 7-ply-thick laminate rather than the nominal 8-ply-thick laminate. For the case where one ply-gap intersects another ply-gap, the shell wall consists of a 6-ply-thick laminate. In addition, these locally thin shell-wall regions have a significant shell-wall mid-surface eccentricity, and have reduced stiffnesses relative to the rest of the shell wall. Magnified cross-sectional views of typical ply-gaps in a -45^o outer ply of a specimen laminate and in a 90^o mid-surface ply are shown in Figs. 4a and 4b, respectively. The widths of the ply-gaps shown in Figs. 4a and 4b are on the order of 0.02 in. or approximately equal to half the shell-wall thickness, and the ply-gap depth is approximately 0.005 in. or approximately equal to the nominal lamina ply thickness. In addition, there often exist regions adjacent to the ply-gaps in which a gradual thickness reduction of the lamina ply occurs as shown in Fig. 4a. These regions of lamina ply thickness reduction can extend an additional 0.02 to 0.04 in. from the edges of the ply-gap. Lamina ply-gaps with gap widths as large as 0.1 in. have been observed in some of the shell specimens. The lighter angular patterns in the thickness contour plot are caused by locally thickened regions of the outermost plies of the laminate that develop during the curing process to form outer shell-wall surface ridges. such as the one shown in Fig. 4c.

Measurements of the top and bottom loading surfaces of the specimens were made every degree around the circumference of the specimens to determine the variation in the shell-end or loading-surface geometry. Typical top and bottom shell-end geometry variations for specimen C3 are denoted by $\delta_{top}(\theta)$ and $\delta_{bot}(\theta)$, respectively, and are shown in Fig. 5. The maximum amplitude of this shell-end variation is approximately 0.0015 inches, which is approximately 4% of t_{ave} or 0.01% of the specimen length.

Test Apparatus and Tests

The specimens were instrumented with electrical resistance strain gages and direct-current differential transducers (DCDT's) were used to measure displacements. Three non-colinear DCDT's were positioned at three corners of the upper loading platen of the test machine and used to measure the end-shortening displacement Δ and the rotations ϕ_y and ϕ_z of the loading platen. These results indicate that significant upper platen rotations occur from the onset of loading up to a load value of approximately 6,000 lbs. These rotations are attributed to an initial misalignment of the upper loading platen and the specimen. The shadow moiré interferometry technique was used to observe the shell-wall prebuckling, buckling and postbuckling normal (perpendicular to the shell outer surface) deformation patterns. All data were recorded with a data acquisition system, and the moiré patterns were recorded photographically and on videotape.

The specimens were loaded in compression with a 300,000-lb hydraulic universal-testing machine. To control the load introduction into the specimens, the upper loading platen was aligned with the loading surface of the specimen as well as possible before the test. The specimens were loaded until general instability of the shells occurred.

Finite-Element Models and Analyses

Nonlinear Analysis Procedure

The shells considered in this study were analyzed with the STAGS (STructural Analysis of General Shells) nonlinear shell analysis code.[12] STAGS is a finite-element code developed for the nonlinear static and dynamic analysis of general shells, and includes the effects of geometric and material nonlinearities in the analysis. The code uses both the modified and full Newton methods for its nonlinear solution algorithms, and accounts for large rotations in a shell by using a co-rotational algorithm at the element level. The Riks pseudo arc-length path-following method[13] is used to continue a solution past the limit points of a nonlinear response. The transient analysis option in STAGS uses proportional structural damping and an implicit numerical time-integration method developed by Park.[14]

The prebuckling, buckling and postbuckling responses of the shells were determined using the following analysis procedure. The prebuckling responses were determined using the geometrically nonlinear quasi-static analysis capability in STAGS. The Riks pseudo arc-length path-following method in STAGS was used to compute the initial shell response until just before buckling occurred. The unstable buckling response of the shell was predicted using the nonlinear transient analysis option of the code. The transient analysis was initiated from an unstable equilibrium state close to the limit point by incrementing the end displacement by a small amount. The transient analysis was continued until the kinetic energy in the shell had dissipated to a negligible level, which indicated that the transient response had attenuated. Once the transient analysis had attenuated to a near-steady-state solution, the load relaxation option of the code was used to establish a static equilibrium state. Conventional linear bifurcation buckling analysis results were also determined with STAGS for comparison with the nonlinear response results.

Finite-Element Models

A typical finite-element model of a specimen is illustrated in Fig. 1. The standard 410 quadrilateral element from the STAGS element library was used in the models. The elements of the finite-element mesh are approximately 0.2-in. by 0.2-in. square. A typical finite-element model contained approximately 100,000 degrees of freedom.

Geometrically perfect and imperfect shells were analyzed in the present investigation. Nominal shell geometry, laminate thickness, lamina mechanical properties, and boundary conditions were used for the finite-element models of the geometrically perfect shells. The nominal boundary conditions consist of setting the circumferential v and normal w displacements equal to zero in the 1.0-in.-long potted boundary regions of the shell illustrated in Fig. 1, setting $u(L/2, \theta) = 0$, and applying a uniform end-shortening $u(-L/2, \theta) = \Delta$. The geometrically perfect finite-element models were modified to include the effects of the measured shell imperfections in order to simulate more closely the response of the specimens. These modeling modifications include the effects of the measured initial geometric shell-wall mid-surface imperfections, shell-wall thickness variations, local shell-wall lamina ply-gaps, thickness-adjusted lamina properties, elastic boundary conditions, shell-end geometric imperfections, and nonuniform end loads.

The effective axial and radial potting-support stiffnesses at the ends of the specimens were determined for each shell specimen to provide a better simulation of the constraints provided by the potting material. A two-dimensional generalized plane-strain finite-element model of the potting-material–shell-wall detail shown in Fig. 6a was used to determine these effective stiffnesses. Material properties of the potting compound were characterized by Iosipescu tests of the potting material reported by Weiland et al.[15] The nominal properties of the potting material are as follows: Young's modulus E = 1.15 Msi, shear modulus G_{12} = 0.36 Msi, and Poisson's ratio ν = 0.59. The effective laminate axial stiffness E_x was used in the shell-wall models which include E_x equal to 11.83, 3.60, and 8.07 Msi, for shells C1, C2 and C3, respectively. To determine the effective axial and radial potting-support stiffnesses, the following numerical experiments were conducted. First, a uniform axial displacement Δ was applied to an unpotted end of the shell model, and the resulting predicted axial strain response, shown in Fig. 6b, was used to calculate an effective axial stiffness K_A for the portions of the shell wall supported by the potting material. The results indicate that the axial strain response of the shell wall supported by the potting material is a function of shell-wall laminate modulus, and that the decay length of the strain response varies inversely with the axial laminate stiffness. The predicted effective axial potted-shell stiffnesses are 26.55, 6.73, and 26.26 Msi for shells C1, C2 and C3, respectively. Then, a unit concentrated force F_z was applied to the shell model, and the resulting w (radial or normal) displacement and nodal force at the junction of the shell wall and the potting material was used to calculate an effective radial support stiffness K_R. The effective radial potting-support stiffness was predicted to be approximately equal to 1.0E5 lbf/in.

Results and Discussion

Analytically predicted and experimentally measured results for the three compression-loaded graphite-epoxy cylindrical shells considered in this study are presented in this section. The results illustrate the effects of initial geometric shell-wall mid-surface imperfections, shell-wall thickness variations and thickness-adjusted lamina properties, local shell-wall lamina ply-gaps, elastic boundary support conditions, and nonuniform loading effects. The results of a comparison between analytically predicted and experimentally measured results are also presented.

Effects of Orthotropy and Anisotropy on the Response of Geometrically Perfect Shells

Results from the nonlinear analyses of geometrically perfect models of shells C1, C2 and C3 are presented in this section. The load-shortening response curves for the shells are compared, and results illustrating a typical nonlinear transient collapse response for the quasi-isotropic shell C3 are presented in detail. Values of the axial load P and the end-shortening Δ presented in this section are normalized by the predicted linear bifurcation buckling load for the quasi-isotropic shell C3, P_{bif}^{quasi} = 42,590 lbs., and the nominal shell-wall thickness, t_{nom} = 0.04 in, respectively.

The predicted load-shortening responses are compared for the three shells in Fig. 7a. The prebuckling load-shortening responses are linear up to the general instability point indicated in the figure for each shell. The prebuckling slopes of each response curve vary according to the individual laminate in-plane axial stiffnesses. General instability occurs at normalized axial load values of 0.707, 0.868, and 0.979, for shells C1, C2 and C3, respectively. The general instability response is followed by a sudden reduction in the axial load supported by the shells which is associated with the transient collapse response of the shells. The corresponding load-time histories of the transient collapse response of the shells are shown in Fig. 7b. The initial portion of a typical load-time history curve, e.g., the one for shell C1, is associated with the transition from a state just before buckling occurs (time = 0.0) to the state associated with the general instability point

indicated in the figure. This initial portion of the load-time history curve only occurs in the analysis of the geometrically perfect shells considered in the present study, and is attributed to the uniformly symmetric character of the initial response. Following the initiation of the general instability response, a typical load-time history curve exhibits a sudden reduction in the axial load supported by the shell which is associated with the transient collapse of the shell. The value of the axial load continues to decrease until the axial load attenuates to a steady-state value. The kinetic energy in the shell dissipates over time and the shell reaches a stable postbuckling equilibrium state after approximately 0.035 to 0.04 seconds have elapsed. Normalized post-collapse postbuckling load values equal to 0.403, 0.218, and 0.286 are obtained for shells C1, C2 and C3, respectively. The results indicate that laminate orthotropy can have a significant effect on the load-shortening response of the shells. In particular, while shell C1 has the lowest general instability load value of all three shells, it also has the highest postbuckling load value of all three shells.

The transient deformation responses for selected time steps during the transient collapse of quasi-isotropic shell C3 are presented in Figs. 8a through 8f. The deformation responses shown in the figures have been scaled for clarity. The shell-wall normal deformations at the general instability point shown in Fig. 7 (0.0125 seconds into the predicted collapse response) change in a short period of time from the uniform axisymmetric prebucking deformation pattern shown in Fig. 8a to the asymmetric transient unstable deformation pattern shown in Fig 8b, at which time the shell begins to collapse. The magnitude of the shell-wall normal displacements varies between ± 0.5 times the shell-wall thickness. The general instability response of the shell is caused by the nonlinear coupling of the localized destabilizing compressive axial and circumferential stresses in the shell indicated in Figs. 9a and 9b and the normal deformations that occur in the bending boundary layer near the ends of the shell. The initial buckling deformation pattern indicated in Fig. 8b is characterized by localized ellipse-like buckles in the bending boundary layer near the ends of the shell. The skewing of the deformation response is attributed to the presence of the small anisotropic bending-twisting coupling stiffness terms of the laminate. After 0.013 seconds have elapsed, the normalized axial load has decreased from 0.983 to 0.479, and the deformation response in the shell has evolved to include additional rows of small ellipse-like buckles as indicated in Fig. 8c. The magnitude of the shell-wall normal displacements vary from +2 to -4 times the shell-wall thickness. After 0.0134 seconds have elapsed, the normalized axial load has decreased to 0.465, and the local buckles in the deformation pattern have rapidly increased in number to include 24 circumferential half-waves and four axial half-waves as indicated in Fig. 8d. After 0.0152 seconds have elapsed, the normalized axial load has decreased further to 0.426, at which time the small buckles in the shell wall begin to coalesce into larger buckles with displacement magnitudes that vary from +3 to -7 times the shell-wall thickness as indicated in Fig. 8e. After approximately 0.04 seconds have elapsed, the kinetic energy in the shell has dissipated to a negligible level, and the shell has deformed into a stable postbuckling mode-shape that consists of 16 circumferential half-waves and two axial half-waves, as indicated in Fig. 8f.

The transient deformation responses for selected time steps during the transient collapse of axially stiff orthotropic shell C1 are presented in Figs. 10a through 10c. The over-all load-time history character of the transient collapse response of shell C1 is similar to that of the response exhibited by shell C3, but there are some differences in the predicted deformation patterns and the collapse initiation events exhibited by shells C1 and C3. The deformation pattern of shell C1 just before buckling occurs is characterized by a uniform short wave-length axisymmetric response along the entire length of the shell as shown in Fig. 10a. These results indicate that the bending boundary layer response does not attenuate for the laminate of shell C1, which is in contrast to the attenuated bending boundary layer response exhibited by shell C3 as shown in Fig 8a. At the general instability point shown in Fig. 7 (after 0.0167 seconds have elapsed in the transient collapse response), a circumferential wave pattern has developed into the shell-wall normal deformations for shell C1 as indicated in Fig. 10b, which is in contrast to the localized response that occurs in the bending boundary layer near the ends of shell C3 as shown in Fig. 8b. The global collapse of shell

C1 initiates in the interior of the shell instead of initiating in the bending boundary layer as did shell C3. In addition, shell C1 does not exhibit the pronounced skewing of the deformation response that was indicated for shell C3, which suggests that this shell is less sensitive to the effects of the small anisotropic bending-twisting coupling stiffness terms of the laminate. After 0.04 seconds have elapsed in the transient collapse response, shell C1 exhibits a postbuckling deformation pattern that is characterized by 16 circumferential half-waves and one axial half-wave as indicated in Fig 10c. This pattern is in contrast to the pattern of shell C3 which has a postbuckling deformation pattern with 16 circumferential half-waves and two axial half-waves.

The transient deformation responses for selected time steps during the transient collapse of circumferentially stiff orthotropic shell C2 are presented in Figs. 11a through 11c. The over-all character of the transient collapse response of shell C2 is similar to the response exhibited by shell C3, however, there are some differences in the resulting deformation patterns exhibited by shell C2. The deformation pattern for shell C2 just before buckling occurs is characterized by a uniform short-wave-length axisymmetric bending boundary layer response that attenuates rapidly into the interior of the shell as shown in Fig. 11a. At the general instability point shown in Fig. 7 (after 0.0217 seconds have elapsed in the transient collapse response), the shell exhibits a deformation pattern that is characterized by one axial half-wave and 22 circumferential half-waves as indicated in Fig 11b. This pattern is in contrast to the short-wave-length responses exhibited by shells C1 and C3 shown in Figs. 10b, and 8b, respectively. In addition, the shell-wall deformations exhibit a significant amount of skewing that is attributed to the presence of the small anisotropic bending-twisting coupling stiffness terms of the laminate. After 0.037 seconds have elapsed in the transient collapse response, shell C2 exhibits a stable postbuckling deformation pattern that is characterized by 14 circumferential half-waves and two axial half-wave as indicated in Fig 11c. This pattern is in contrast to the pattern for shell C3 which exhibits a postbuckling deformation pattern with 16 circumferential half-waves and two axial half-waves.

The previous results indicate that laminate orthotropy can have an effect on the nonlinear response of compression-loaded composite shells. In particular, the results indicate that the bending boundary layer attenuation response can be significantly affected by the orthotropy of the laminate. The effects of laminate orthotropy on the displacement profiles just before buckling occurs are indicated in Fig. 12 for the three shells. The dashed, dash-dot, and solid lines represent displacement profiles for shells C1, C2 and C3, respectively. These results indicate that the axially stiff orthotropic shell C1 exhibits large-amplitude short-wave-length bending deformations just before buckling occurs. In addition, the bending response decays only slightly over the length of this shell. In contrast, shells C2 and C3 exhibit short-wave-length bending boundary layer responses that attenuate into the interior of the shell. These results also indicate that the laminate orthotropy can have a significant effect on the magnitude of the maximum displacements in the bending boundary layer near the ends of the shell. The displacements with the largest magnitude are exhibited by shell C1 which has a maximum displacement magnitude of approximately 0.34 w/t_{nom} followed by shells C2 and C3 which have maximum displacement magnitudes equal to 0.29 and 0.24 w/t_{nom}, respectively. Additional results are presented in Fig. 13 that indicate the effects of shell length on the bending boundary layer attenuation characteristics of shell C1. The solid, dashed, and dash-dot lines in the figure represent displacement profiles for shell length-to-radius ratios L/R equal to 2, 3 and 4, respectively. These results indicate that the bending boundary layer response for the shell C1 laminate attenuates for the longer shells, but not for the shorter shell. In addition, the results indicate that the magnitude of the large-amplitude displacements near the ends of the shell decreases as the length of the shell increases. These results suggest that the non-attenuating bending boundary layers in the shorter shell interact to cause displacements with larger magnitudes in this shell. These results also suggest that the effects of the attenuation length of the bending boundary layer should be considered in studies of the nonlinear stability response of orthotropic shells and in the design of these shells.

Effects of Initial Imperfections on the Buckling Response

Typical analytically predicted transient response deformations that occur during the collapse of shell C3 with measured imperfections included in the analysis are shown in Figs. 14a through 14d. Just before buckling occurs, the shell wall deformations are characterized by several localized ellipse-like deformation patterns as indicated in Fig. 14a. The localization in the deformation pattern is caused by the combination of a local geometric shell-wall imperfection that is in the form of a significant variation in the shell-wall mid-surface geometry, and the intersection of a helical ply-gap and a circumferentially aligned ply-gap in the shell at $x/L_T = 0.25$ and $\theta = 210^o$. The localized deformations occur in regions with destabilizing compressive axial and circumferential stresses as indicated in Fig. 15. After approximately 0.00143 seconds have elapsed in the transient response, a single ellipse-like buckle has grown in amplitude and couples with the destabilizing stresses in the shell wall to cause the general instability and collapse of the shell. After approximately 0.00238 seconds have elapsed in the transient response, additional local buckles have formed around the circumference and along the length of the shell as indicated in Fig. 14c. As the buckling process continues, the deformation pattern in the shell wall continues to evolve and the ellipse-like buckles in the shell begin to coalesce into larger diamond-shaped buckles. After approximately 0.02 seconds have elapsed in the transient response, the kinetic energy in the shell has dissipated to a negligible level, and the shell has deformed into a stable postbuckling mode-shape as indicated in Fig. 14d. These results indicate that the collapse response of the imperfect shell is initiated by a localized response which leads to the overall collapse of the shell. These results are different from the collapse response results exhibited by the corresponding geometrically perfect shell which are shown in Figs. 8a-8f. The transient collapse response occurs after 0.00143 seconds have elapsed in the transient analysis in the shell with imperfections, and this collapse response occurs much earlier than for the corresponding geometrically perfect shell collapse response. This earlier collapse time is attributed to the localized prebuckling shell-wall deformations and destabilizing in-plane compressive stresses in the shell, which result in a rapid transition from the stable prebuckling state to the unstable transient collapse response. Results for orthotropic shells C1 and C2 indicate similar response characteristics associated with the transient collapse response of these shells.

Effects of Lamina Ply-Gap Fabrication Defects

Selected results illustrating the effects of lamina ply-gaps on the response of quasi-isotropic shell C3 are presented in this section. First, results illustrating the effects of lamina ply-gap orientation, ply-gap width, and ply-gap depth on the buckling load of this shell are presented. Ply-gap orientations of -45^o, $+45^o$, 0^o, and 90^o; ply-gap widths equal to 0.1 in., and 0.2 in.; and ply-gap depths equal to 0.005 in. and 0.0025 in. are considered. Then, typical results illustrating the effects of a helical ply-gap on the transient collapse response of the shell are presented.

Results illustrating the effects of ply-gap orientation, width, and depth on the buckling load of shell C3 are shown in Fig. 16 where the buckling load P_{cr} is normalized by the linear bifurcation buckling load P_{bif}. The open square symbols represent calculated normalized buckling loads. The solid and dashed lines represent result trends for ply-gap depths of 0.005 in. and 0.0025 in., respectively. The results indicate that the buckling load of the quasi-isotropic shell can be affected by certain types of lamina ply-gaps. In general, as the ply-gap width and ply-gap depth are increased, the buckling load decreases. The results also indicate that the buckling load is sensitive to the orientation of the ply-gap. These results indicate that shells with 90^o ply-gaps exhibit the most significant reductions in buckling load followed by shells with -45^o, $+45^o$ and 0^o ply-gaps. The results also indicate that shells with -45^o ply-gaps exhibit lower buckling loads than shells with $+45^o$ ply-gaps. These results suggest that there is a nonlinear coupling response that

is affected by the laminate anisotropy and the local structural response associated with the lamina ply-gap. In addition, the results indicate that the buckling load of the shell is not sensitive to the effects of a 0^o ply-gap. The benign effect of the 0^o ply-gap suggests that the local bending deformations and destabilizing in-plane stresses near the ply-gap for this shell do not significantly affect the buckling of the shell.

Transient deformation response results for selected time steps during the transient collapse of quasi-isotropic shell C3 with a -45^o lamina ply-gap are presented in Fig. 17a through 17d. Just before buckling occurs, the shell-wall deformations are characterized by a combination of a large local inward deformation pattern aligned with the ply-gap and a small ellipse-shaped deformation pattern located at the intersection of the bending boundary layer deformations near the end of the shell and the ply-gap as shown in Fig. 17a. The destabilizing in-plane axial and circumferential stresses shown in Fig. 18a and 18b, respectively, couple with the normal shell-wall deformations to cause the general instability and collapse of the shell to occur. After approximately 0.0012 seconds have elapsed in the transient response, additional ellipse-like or diamond-shaped buckle patterns have formed in the shell in the vicinity of the ply-gap as indicated in Fig. 17b. After approximately 0.0029 seconds have elapsed in the transient response, additional local buckle patterns have formed around the circumference and along the length of the shell as indicated in Fig. 17c. As the buckling process continues, the deformation pattern in the shell-wall continues to evolve, and the ellipse-like buckle patterns in the shell begin to coalesce into larger diamond-shaped buckle patterns. After approximately 0.02 seconds have elapsed in the transient response, the kinetic energy in the shell has dissipated to a negligible level, and the shell has deformed into a stable postbuckling mode-shape as indicated in Fig. 17d. Similar results for orthotropic shells C1 and C2 indicate that the nonlinear response and buckling loads of these orthotropic shells are only slightly affected by the lamina ply-gap features. For these orthotropic shells, the ply-gaps cause a maximum reduction in the predicted buckling loads of approximately 1-2%. This benign effect of the ply-gaps on the buckling loads of these orthotropic shells suggests that the local bending deformations and destabilizing in-plane stresses associated with the ply-gaps do not significantly affect the buckling loads of these shells.

Effects of Elastic Boundary Conditions

The potting material applied to the ends of the shell specimens is intended to prevent premature damage to the ends of the shell during testing. In practice, it is virtually impossible to achieve perfect rigidly clamped supports in a test. It has been shown by Fuchs et al.[16] that the displacement and strain responses in cylindrical shells subjected to an applied bending load can be sensitive to the flexibility of the specimen support conditions. To determine if the flexibility of the end supports may affect the response of compression-loaded shells, an analytical study was conducted to assess the effects of axial and radial potting-support stiffnesses on the response of the shells considered in the present study. Preliminary results indicate that the axial potting-support stiffness primarily affects the effective axial stiffness of the shell and has no noticeable effect on the displacement and strain response of the shell. However, the results also indicate that the radial potting-support stiffnesses can have a significant effect on the displacement and strain response of the shells, and some of these results are presented herein.

Selected results from a parametric study are presented to illustrate the effects of elastic radial constraints on the displacement and strain response of selected geometrically perfect and imperfect shells. Elastic radial stiffnesses K_R equal to 1.0E3, 1.0E5, and 1.0E7 lbf/in. were considered in the study. A value of the elastic radial stiffness K_R = 1.0E5 lbf/in. corresponds to the effective radial potting-support stiffness calculated from the potting model illustrated in Fig. 6, and a value of K_R = 1.0E7 lbf/in. corresponds to a clamped condition. Results illustrating the effects of elastic radial potting-support conditions on typical prebuckling normal or radial displacements of geometrically perfect and imperfect orthotropic shell C2 are

presented in Figs. 19a and 19b, respectively. The normal displacement w and the axial coordinate x are normalized with respect to the nominal shell-wall thickness t_{nom} and the shell test-section length L_T, respectively. The solid, dashed, and dot-dashed lines in the figures represent results for shells with elastic radial potting-support stiffnesses K_R equal to 1.0E7, 1.0E5, and 1.0E3 lbf/in., respectively. The results indicate that the variation in the radial boundary stiffness can have a measurable effect on the magnitude of the displacements for the geometrically perfect shell as shown in Fig. 19a. These results indicate that radial boundary stiffnesses equal to 1.0E5 and 1.0E7 lbf/in. restrain the radial displacements at the boundaries of the shell. However, when the elastic radial boundary stiffness is reduced to 1.0E3 lbf/in., the boundaries of the shell have an outward radial displacement of approximately 0.06 w/t_{nom} and a reduction in the maximum displacements in the bending boundary layer of approximately 0.02 w/t_{nom}. In addition, the shell exhibits a slight axial shift in the bending boundary layer response near the ends of the shell. These results indicate that the variation in radial boundary stiffness can have a significant effect on the displacement response of a shell with imperfections as shown in Fig. 19b. The results indicate that there can be a 20 to 25% variation in the local displacement response at several locations along the length of the shell for the different boundary conditions. Other related results indicate that these variations in the radial boundary stiffness and variations in the prebuckling displacement response can cause significant changes in the character of the collapse and post-collapse deformation responses of the shells.

Effects of Uncertainties or Variations in Selected Specimen Parameters

Results from a numerical study of the effects of uncertainties or variations of selected specimen parameters on the response of the imperfect quasi-isotropic shell C3 are presented in this section. The parametric uncertainties considered include uncertainties in the imperfection measurements, the lamina fiber volume fraction, and the applied load distribution. The imperfection measurement uncertainties are attributed to the accuracy tolerances of the coordinate measurement device used to measure the initial geometry of the shell. The shell-wall imperfection measurement values and the shell-end-shape imperfection measurement values used in the present study are accurate to within ± 0.0006 inches, or $\pm 0.75\text{E-}4R$ and $\pm 1.5\text{E-}4L$. The shell-wall thickness values are accurate to within ± 0.0012 inches, or $\pm 0.03 t_{nom}$. The lamina fiber volume fraction is specified by the manufacturer of the material to be equal to 0.65 ± 0.03 for the 0.005-in.-thick graphite-epoxy preimpregnated tape material used to fabricate the test specimens. Applied load distribution uncertainties are measured indirectly by monitoring the measured and predicted axial strains at selected points near the top and bottom loading surfaces of the shell. The parameter uncertainties considered in this study include variations in the lamina fiber volume fraction, the measured shell-wall thickness imperfection, and the applied load distribution. Trends in the results for shells with thickness imperfection measurement variations of -3%, 0%, and +3%, respectively, indicate that the normalized buckling loads range from 0.83 to 1.0, and that variations in these parameters can have a significant effect on the buckling load of the shell. In particular, the results indicate that a variation in the shell wall thickness of $\pm 3\%$ can result in a 6% variation in the buckling load of the shell. Similarly, results indicate that a $\pm 3\%$ variation in the fiber volume fraction can result in an 8% variation in the buckling load.

Predicted and Measured Response Comparisons

Selected results from nonlinear analyses of the orthotropic and quasi-isotropic shells are compared to the experimentally measured results in this section. The nonlinear analysis results are for shell models that included the effects of the measured initial shell-wall geometric and thickness imperfections, thickness-adjusted material property variations, shell-wall lamina ply-gaps, measured loading variations, elastic radial support conditions, and selected specimen parameter uncertainties. A value of the elastic radial support stiffness equal to 1.0E5 lbf/in. is used in the models to simulate the boundary conditions provided by

the potted-end supports of the shell specimens. Upper and lower response bounds were determined based upon the results of a traditional combinatorial analysis of the effects of selected specimen parameter uncertainties. Uncertainties in the measured thickness imperfection, lamina fiber volume fraction, and applied load distribution were considered in the analysis. Predicted and measured load-shortening response curves and selected load-strain responses are presented in this section.

Analytically predicted and experimentally measured load-shortening response curves for shells C1, C2 and C3 are presented in Fig. 20. Values of the axial load P and the end-shortening Δ are normalized by the linear bifurcation buckling load of quasi-isotropic shell C3, P_{bif}^{quasi} = 42,590 lbs., and the nominal shell-wall thickness t_{nom} = 0.04 in, respectively. The solid and dashed lines in the figure represent experimentally measured and analytically predicted results, respectively. Each shell has two predicted response curves representing analytically predicted upper and lower bounds to the response based on specimen parameter uncertainties. The measured results indicate that shells C1, C2 and C3 exhibit the general instability points shown in the figure at normalized load values of 0.652, 0.749, and 0.803, respectively, and are 7.8, 13.7, and 17.6% lower than the predicted loads for the geometrically perfect nominal shells shown in Fig. 7a, respectively. These results indicate that, for the most part, the measured load-shortening response curves for the shells fall on or within the analytically predicted response bounds. These results indicate that the measured response curves tend to correlate well with the analytically predicted lower bounds for each shell.

Predicted initial post-collapse normal displacement contours and the corresponding observed moiré fringe patterns for specimen C1 are shown in Fig. 27. The dashed contour lines in the predicted displacement contour plots represent inward displacements and the solid lines represent outward displacements. The density of the contour lines indicates the severity of the displacement gradients in the specimen. These results indicate that the specimen collapses into a general-instability diamond-shaped buckling pattern with 16 half-waves around the circumference and one half-wave along the length, as predicted by the transient analysis. Predicted initial post-collapse normal displacement contours and the corresponding observed moiré fringe patterns for specimen C2 are shown in Fig. 22. These results indicate that the specimen collapses into a general instability diamond-shaped buckling pattern with 14 half-waves around the circumference and two half-waves along the length, as predicted by the transient analysis. Similar results for shell C3 indicate that the shell collapses into a general-instability diamond-shaped pattern with 16 circumferential half-waves and two axial half waves.

Design Considerations

The nonlinear analysis procedure described herein offers a robust and accurate approach for predicting the nonlinear response and stability characteristics of compression-loaded thin-walled composite shell structures. This nonlinear analysis procedure can be used to form the basis of a modern high-fidelity design and analysis approach for composite shell structures that accounts for the effects of imperfections associated with the fabrication process used to fabricate the structure. A comparison of results from the traditional shell design approach and from the present nonlinear high-fidelity shell design approach is shown in Fig. 23 for shell C3. Values of the axial load P and the end-shortening Δ in the figure are normalized by the predicted linear bifurcation buckling load for quasi-isotropic shell C3, P_{bif}^{quasi} = 42,590 lbs., and the nominal shell-wall thickness t_{nom} = 0.04 in, respectively. The traditional approach to shell design is to predict the shell buckling load using a linear bifurcation buckling analysis with the nominal structural dimensions and material properties of an idealized geometrically prefect shell. This predicted bucking load for the shell is then reduced by an empirical “knockdown” factor based on a design criterion such as the lower-bound design recommendations reported in NASA SP-8007 (Ref. 1). Quasi-isotropic shell C3 has

a nominal radius-to-shell-wall-thickness ratio equal to 200, and the design knockdown factor from NASA SP-8007 for an equivalent isotropic shell is approximately equal to 0.470 as indicated in Fig. 30. This traditional design approach results in an overly conservative design for this shell. The normalized measured buckling load and the normalized predicted buckling load from the lower response bound predicted by the nonlinear analysis procedure are 0.803 and 0.832, respectively, and these results are approximately 33 and 36% greater than the results based on the traditional design approach. The modern high-fidelity analysis approach offers a relatively affordable alternative to relying on historical test data for shells that do not represent the configuration, material system, or fabrication process for a particular composite shell design of interest. This suggested design analysis procedure should be used with a selected number of carefully conducted experiments that would be used to verify the design and analysis results. This approach would make it possible to avoid testing the large number of replicates of a design needed to develop empirical design factors. This nonlinear analysis procedure could be used as a parametric tool in the early stages of a design development program to determine the sensitivity of the response characteristics of a specific design to a number of different types of imperfections or differences in the idealized as-designed shell structure and the actual as-manufactured shell structure.

Concluding Remarks

The results of an experimental and analytical study of the effects of imperfections on the nonlinear response and buckling loads of unstiffened thin-walled compression-loaded graphite-epoxy cylindrical shells with three shell-wall laminates are presented. The shell-wall laminates considered in this study include a quasi-isotropic laminate and two different orthotropic laminates. The results for the nonlinear prebuckling, buckling, transient collapse, and post-collapse response of geometrically perfect shells and shells with measured imperfections are presented. The results identify the effects of traditional initial geometric shell-wall mid-surface imperfections and the effects of other nontraditional imperfections on the nonlinear response and buckling loads of the shells. These nontraditional imperfections include shell-wall thickness variations, material property variations, shell-end geometric imperfections, local shell-wall ply-gaps associated with the fabrication process, variations in loads applied to the end of the shell, and elastic boundary support conditions. In addition, upper and lower bounds to the nonlinear response of the shells have been determined based on a combinatorial analysis of the effects of uncertainties or variations in several shell parameter are presented. A high-fidelity nonlinear shell analysis procedure has been used to predict the nonlinear response of the shells, and the analysis procedure accurately accounts for the effects of these traditional and nontraditional imperfections and elastic boundary conditions on the nonlinear response and buckling loads of the shells. The analysis results generally correlate well with the experimental results indicating that it is possible to predict accurately the complex nonlinear response and buckling loads for compression-loaded composite shell structures when the traditional and nontraditional imperfections considered in the present study are included in the analysis.

The analytical results indicate that the effects of the traditional and nontraditional imperfections considered in this study can be important for predicting the buckling loads of composite shells since they can significantly affect the nonlinear response and buckling loads of the shells. The results indicate that the measured imperfections can couple with the in-plane compressive stress resultants in a nonlinear manor to affect the shell response. The results show that shell-wall laminate orthotropy can also have a significant effect on the nonlinear response and buckling loads of composite shell structures, and that the buckling loads of the orthotropic shells studied are less sensitive to the effects of the measured imperfections considered in this study than is the buckling load of the quasi-isotropic shell studied. In addition, the results indicate that elastic boundary support conditions can have a significant effect on the displacement and strain responses of the shells, shell length and shell-wall orthotropy can have a significant effect on the attenuation of the shell-end bending boundary layer, and shell-wall ply-gaps associated with the fabrication

process can have a significant effect on the shell buckling loads.

The results of the study indicate that, for the most part, the measured response of the shells falls on or within the predicted upper and lower bounds to the response that are associated with the uncertainties or variations in the shell parameters considered in the study. These results indicate that the nonlinear analysis procedure used in this study can be used to determine accurate, high-fidelity design knockdown factors that can be used for predicting composite shell buckling and collapse loads in the design process. The traditional and nontraditional imperfections considered in this study could be used to formulate the basis for a generalized imperfection signature of a composite shell. This generalized imperfection signature would include the effects of variations or uncertainties in the shell-geometry, fabrication-process, load-distribution and boundary stiffness parameters. The high-fidelity nonlinear analysis procedure used in this study can be used to form the basis for a shell analysis and design approach that includes this generalized imperfection signature. Furthermore, a high-fidelity analysis procedure can be used to addresses some of the critical shell-buckling design criteria and design considerations for composite shell structures without resorting to the traditional empirical shell design approach that leads to overly conservative designs.

References

1. Anon., Buckling of Thin-Walled Circular Cylinders. NASA Space Vehicle Design Criteria, NASA SP-8007, September 1965.

2. Koiter, W. T., "On the Stability of Elastic Equilibrium," (in Dutch), H. J. Paris, Amsterdam, Holland, 1945; translation available as AFFDL-TR-70-25, February 1970, Wright-Patterson Air Force Base.

3. von Kármán, T. and Tsien, H-S., "The Buckling of Thin Cylindrical Shells Under Axial Compression," *Journal of the Aeronautical Science*, Vol. 8, No. 8, June 1941, pp. 303-312.

4. Budiansky, B. and Hutchinson, J., "Dynamic Buckling of Imperfection Sensitive Structures," Proceedings of the 11th IUTAM Congress, H. Gortler, Ed., Springer-Verlag, Berlin, 1964, pp. 636-651.

5. Árbocz, J. and Babcock, C. D., "The Effect of General Imperfections on the Buckling of Cylindrical Shells," *Journal of Applied Mechanics*, Vol. 36, Series E, No. 1, 1969, pp. 28-38.

6. Sechler, E. E., "The Historical Development of Shell Research and Design," in *Thin-Shell Structures, Theory, Experiments and Design*, Fung, Y. C. and Sechler, E. E., Eds., Prentice-Hall, Englewood Cliffs, NJ, 1974, pp. 3-25.

7. Árbocz, J., "The Effects of Imperfect Boundary Conditions on the Collapse Behavior of Anisotropic Shells," Proceedings of the Joint Applied Mechanics and Materials ASME Summer Conference, AMD-MD'95, Los Angeles, CA, June 28-30, 1995.

8. Árbocz, J., Starnes, J. H., Jr., and Nemeth, M. P., "A Hierarchical Approach to Buckling Load Calculations," Proceedings of the 40th AIAA/ASME/ASCE/AHS/ASC Structures, Structural Dynamics and Materials Conference, St. Louis, MO, 1999. AIAA Paper No. 99-1232.

9. Koiter, W. T., Elishakoff, I., Li, Y. W., and Starnes, J. H., Jr., "Buckling of an Axially Compressed Imperfect Cylindrical Shell of Variable Thickness," Proceedings of the 35th AIAA/ASME/ASCE/AHS/ASC Structures, Structural Dynamics and Materials Conference, Hilton Head, SC, 1994. AIAA Paper No. 94-1339.

10. Starnes, J. H., Jr., Hilburger, M. W., and Nemeth, M. P., "The Effects of Initial Imperfections on the Buckling of Composite Shells," *Composite Structures: Theory and Practice*, ASTM STP 1383, P. Grant and C. Q. Rousseau, Eds., American Society for Testing and Materials, 2000, pp. 529-550.

11. Hilburger, M. H., and Starnes, J. H., Jr., "Effects of Imperfections on the Buckling Response of Compression-loaded Composite Shells," Proceedings of the 41st AIAA/ASME/ASCE/AHS/ASC Structures, Structural Dynamics, and Materials Conference, Atlanta, GA, 2000. AIAA Paper No. 2000-1387.

12. Rankin, C. C., Brogan, F. A., Loden, W. A., and Cabiness, H. D., "STAGS Users Manual, Version 3.0," Lockheed Martin Missiles & Space Co., Inc., Advanced Technology Center, Report LMSC P032594, 1999.

13. Riks, E., "Progress in Collapse Analysis," *Journal of Pressure Vessel Technology*, Vol. 109, 1987, pp. 27-41.

14. Park, K. C., "An Improved Stiffly Stable Method for Direct Integration of Nonlinear Structural Dynamics," *Journal of Applied Mechanics*, Vol. 42, June 1975, pp. 464-470.

15. Weiland, T. M., Morton, J., and Starnes, J.H., "Scaling Effects in Buckling, Postbuckling and Crippling of Graphite-Epoxy Z-Section Stiffeners," Virginia Polytechnic Institute and State University, Report CCMS-92-25, September 1992.

16. Fuchs, J. P., Hyer, M. W., and Starnes, J. H., "Numerical and Experimental Investigation of the Bending Response of Thin-Walled Composite Cylinders," Virginia Polytechnic Institute and State University, Report CCMS-93-19/VPI-E-93-11, September 1993.

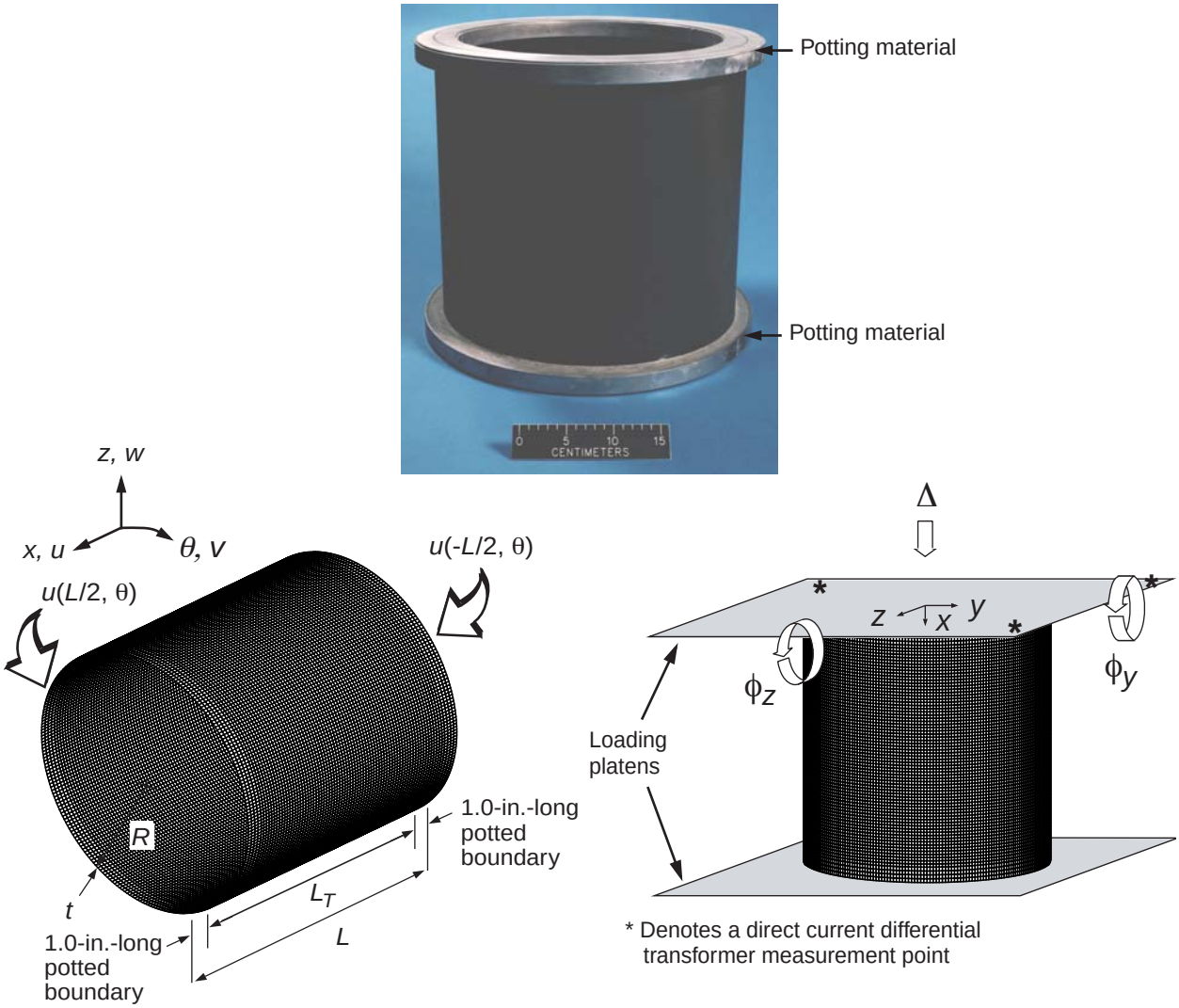

Fig. 1 Typical specimen and finite-element model geometry.

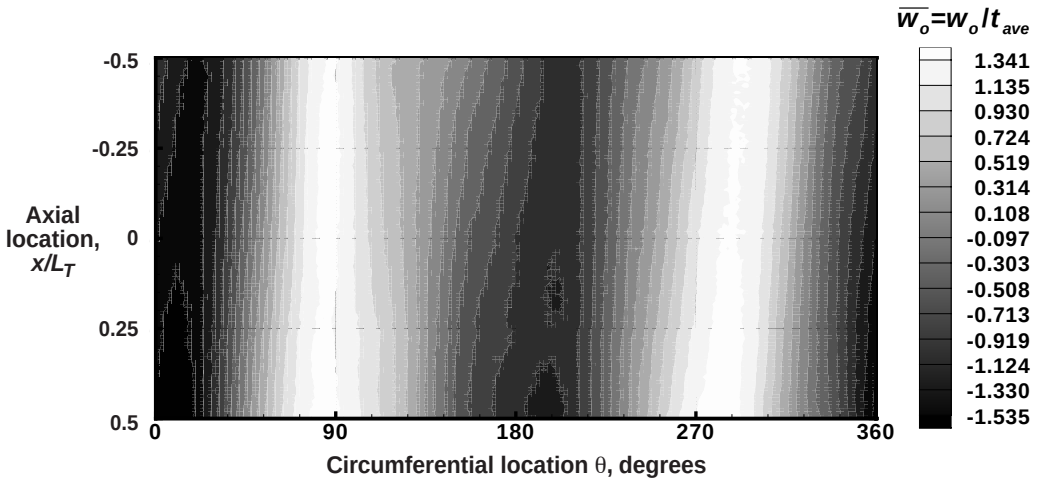

Fig. 2 Typical measured inner-surface imperfection shape for shell specimen C3.

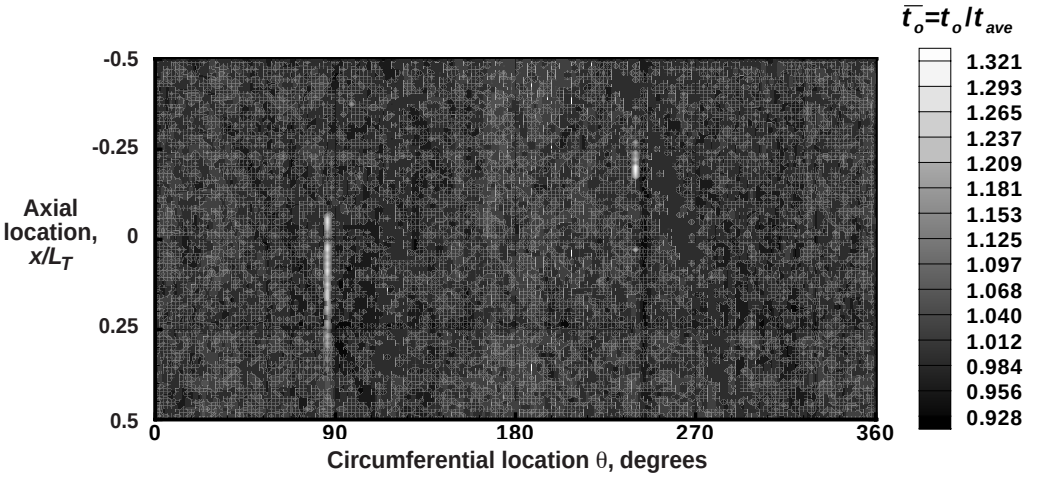

Fig. 3 Typical measured wall thickness variation for a shell specimen C3.

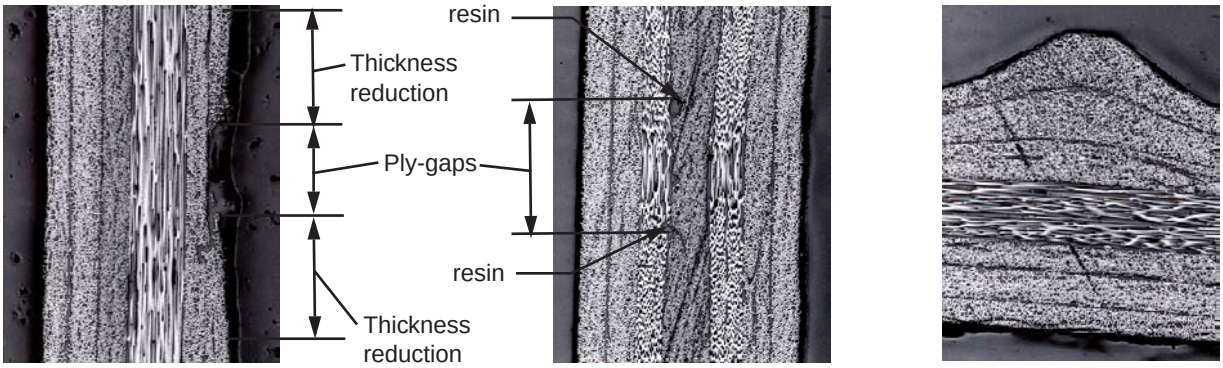

a) Ply-gap in a 45° outer-surface lamina ply

b) Ply-gap in a 90° inner-surface lamina ply

c) Outer-surface ridge

Fig. 4 Magnified cross-sectional views of lamina ply-gaps and a magnified cross-sectional view of an outer-surface ridge.

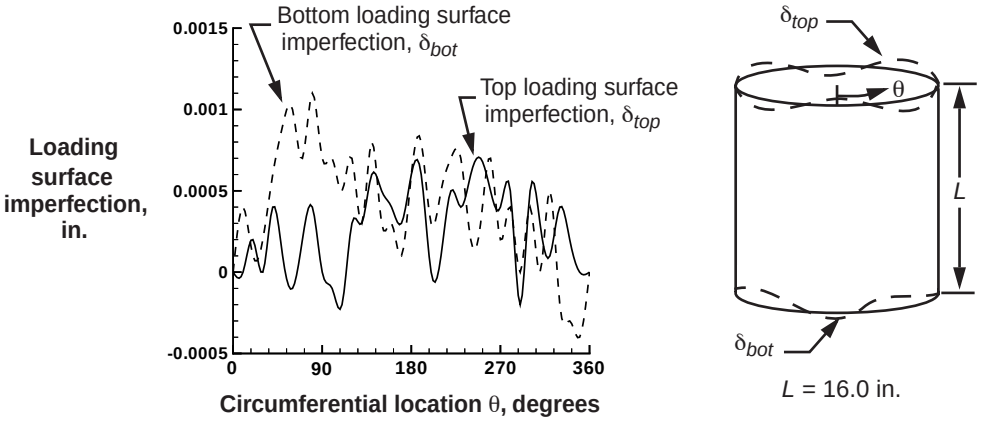

Fig. 5 Typical measured shell-end or loading-surface imperfections for a shell specimen C3.

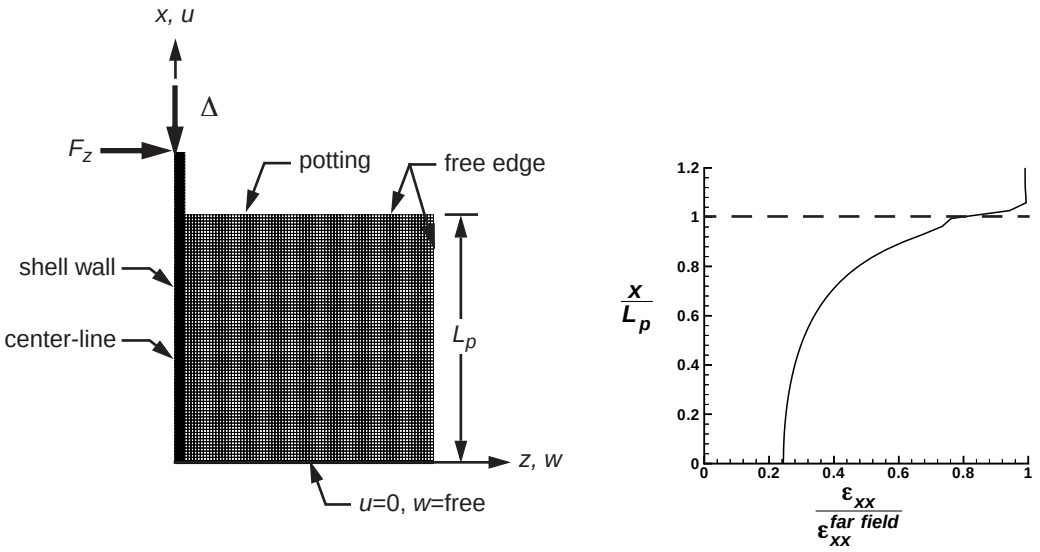

Fig. 6 Typical finite-element model and geometry and boundary conditions of the potting-shell detail and typical predicted axial strain distribution at the mid-surface of the shell wall.

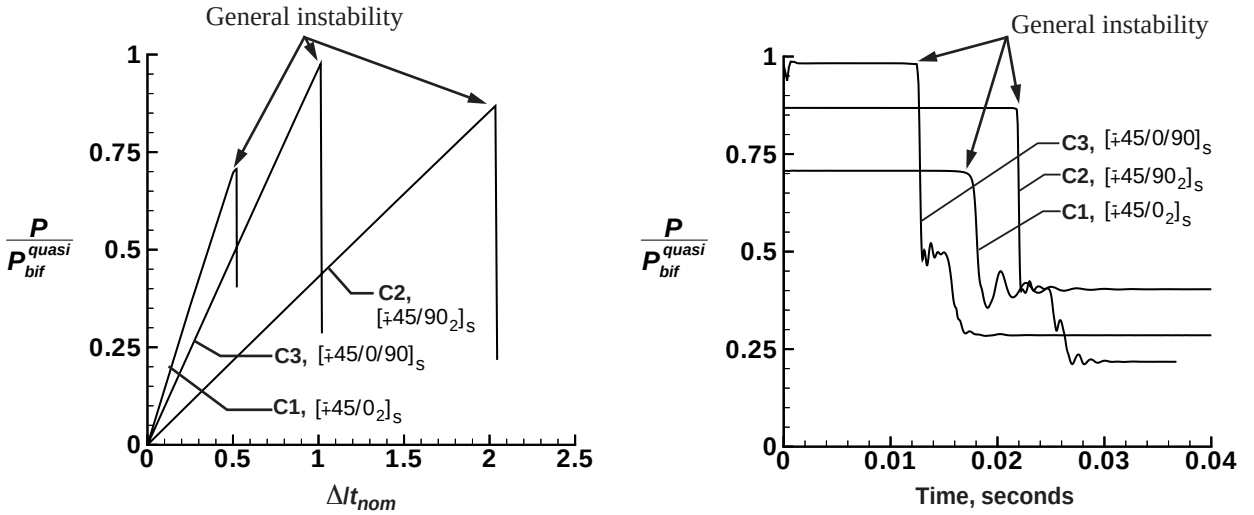

a) Normalized load-shortening response curves

b) Normalized load-time history during collapse

Fig. 7 Numerically predicted nonlinear response of geometrically perfect compression-loaded cylindrical shells.

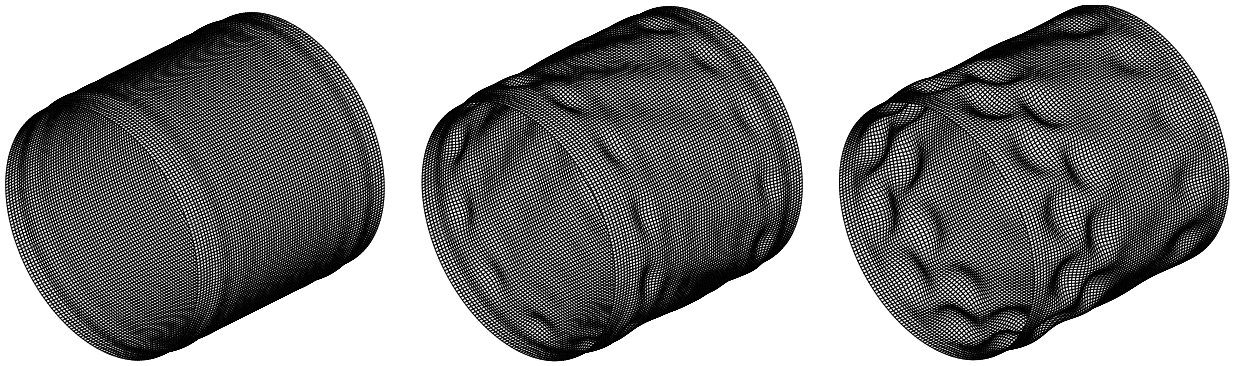

a) Prebuckling deformations
Time = 0.0 seconds
P/P_{bif}^{quasi} = 0.979

b) Initial collapse deformations
Time = 0.0125 seconds
P/P_{bif}^{quasi} = 0.983

c) Transient collapse deformations
Time = 0.0130 seconds
P/P_{bif}^{quasi} = 0.479

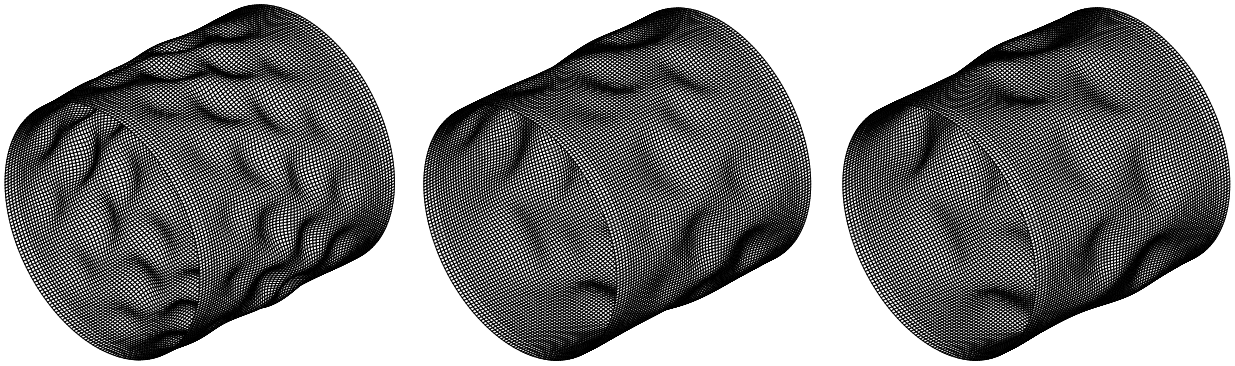

d) Transient collapse deformations
Time = 0.0134 seconds
P/P_{bif}^{quasi} = 0.465

e) Transient collapse deformations
Time = 0.0152 seconds
P/P_{bif}^{quasi} = 0.426

f) Post-collapse
Time = 0.04 seconds
P/P_{bif}^{quasi} = 0.286

Fig. 8 Numerically predicted collapse response for a geometrically perfect compression-loaded quasi-isotropic shell C3.

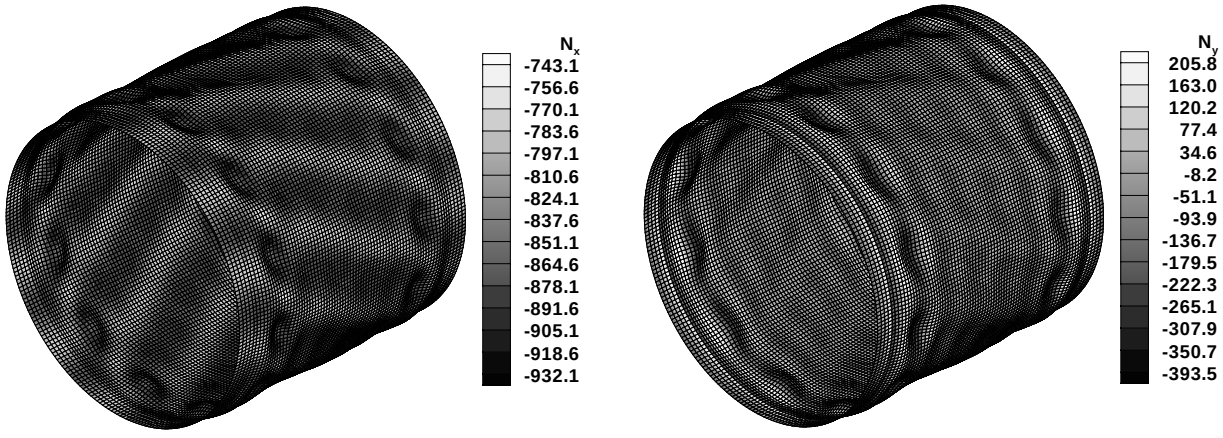

a) Axial stress resultant contours, N_x, lbf/in

b) Circumferential stress resultant contours, N_y, lbf/in

Fig. 9 Numerically predicted axial and circumferential stress resultants, N_x and N_y, respectively, just before buckling for a geometrically perfect compression-loaded quasi-isotropic shell C3.

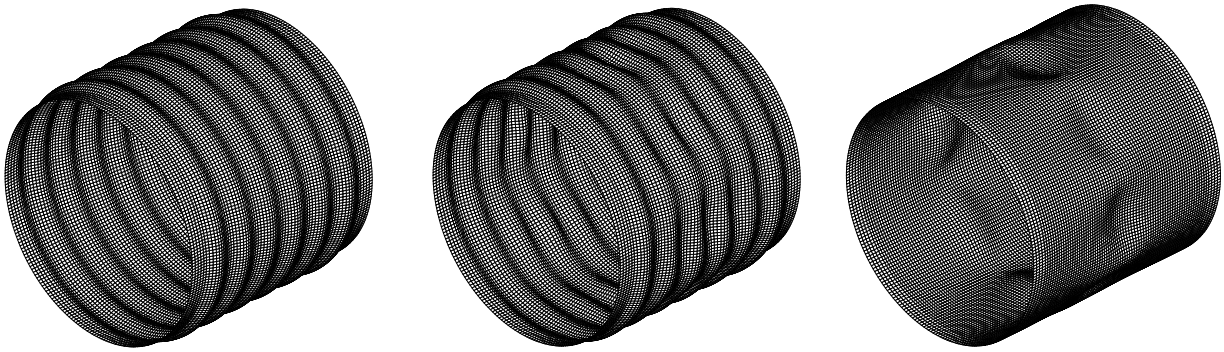

a) Prebuckling deformations
Time = 0.0 seconds
$P/P_{bif}^{quasi} = 0.707$

b) Initial collapse deformations
Time = 0.0167 seconds
$P/P_{bif}^{quasi} = 0.704$

c) Post-collapse deformations
Time = 0.04 seconds
$P/P_{bif}^{quasi} = 0.403$

Fig. 10 Numerically predicted collapse response for a geometrically perfect compression-loaded orthotropic shell C1.

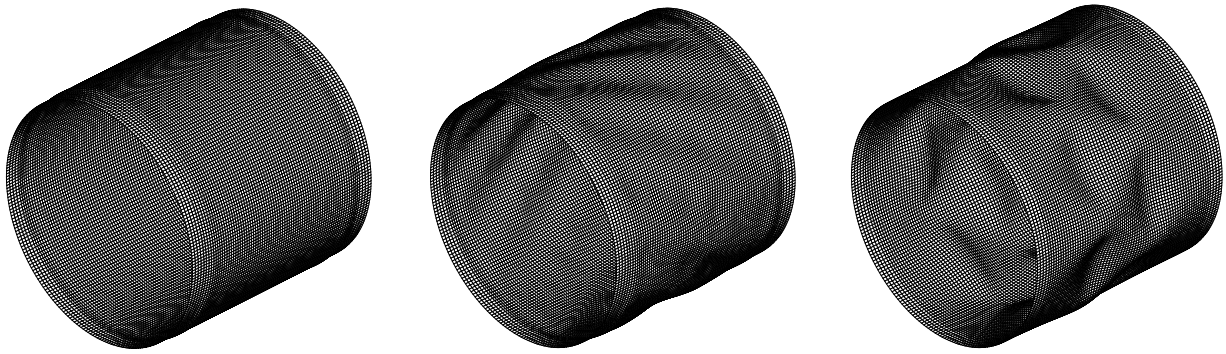

a) Prebuckling deformations
Time = 0.0 seconds
$P/P_{bif}^{quasi} = 0.868$

b) Initial collapse deformations
Time = 0.0217 seconds
$P/P_{bif}^{quasi} = 0.866$

c) Post-collapse
Time = 0.037 seconds
$P/P_{bif}^{quasi} = 0.218$

Fig. 11 Numerically predicted collapse response for a geometrically perfect compression-loaded orthotropic shell C2.

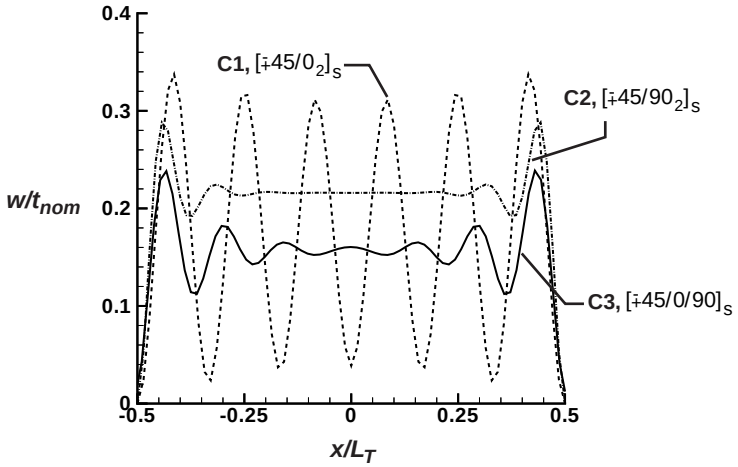

Fig. 12 Effects of orthotropy on displacements just before buckling of geometrically perfect compression-loaded composite cylindrical shells.

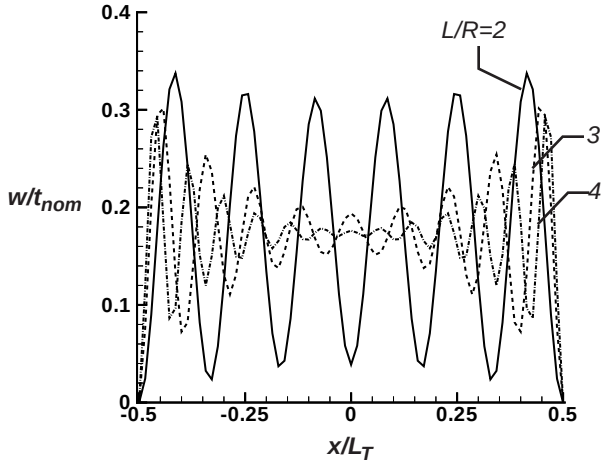

Fig. 13 Effects of shell length on bending boundary layer attenuation for a geometrically perfect compression-loaded orthotropic shell C1.

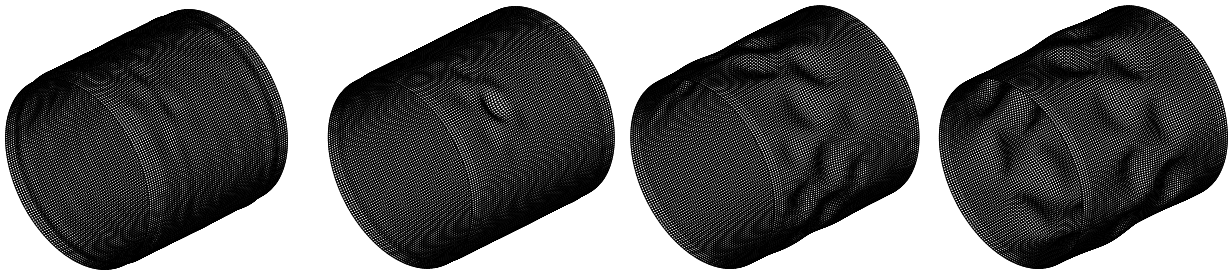

a) Prebuckling deformations
Time = 0.0 seconds
P/P_{cr} = 0.858

b) Initial collapse deformations
Time = 0.00143 seconds
P/P_{cr} = 0.855

c) Transient collapse deformations
Time = 0.00238 seconds
P/P_{cr} = 0.598

d) Post-collapse deformations
Time = 0.02 seconds
P/P_{cr} = 0.311

Fig. 14 Numerically predicted collapse response for an imperfect compression-loaded quasi-isotropic shell C3.

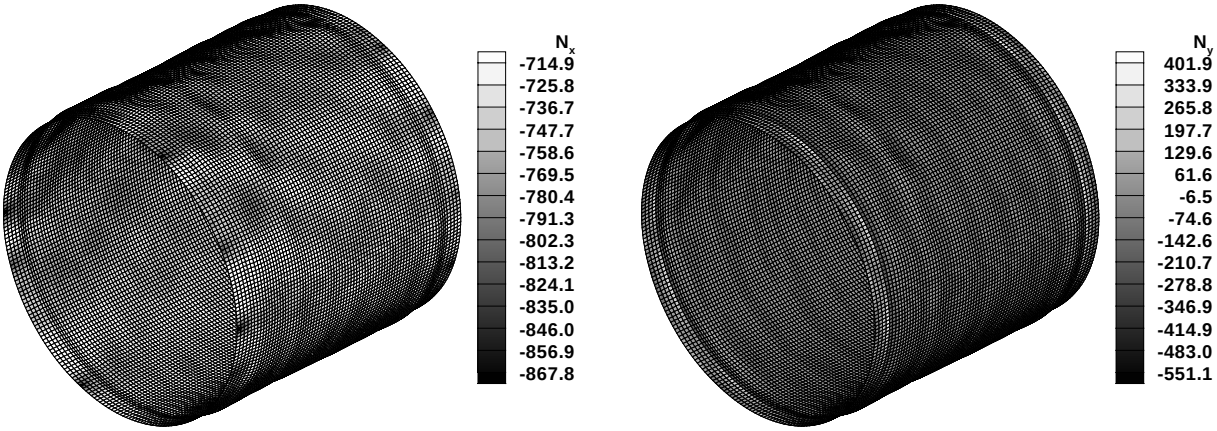

a) Axial stress resultant contours, N_x, lbf/in.

b) Circumferential stress resultant contours, N_y, lbf/in.

Fig. 15 Numerically predicted axial and circumferential stress resultants, N_x and N_y, respectively, just before buckling for an imperfect compression-loaded quasi-isotropic shell C3.

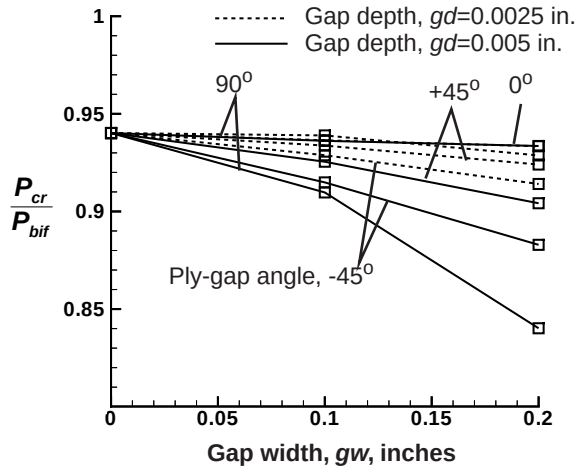

Fig. 16 Effects of ply-gap angle, gap width *gw*, and gap depth *gd*, on the normalized buckling load of a geometrically perfect compression-loaded quasi-isotropic cylindrical shell C3.

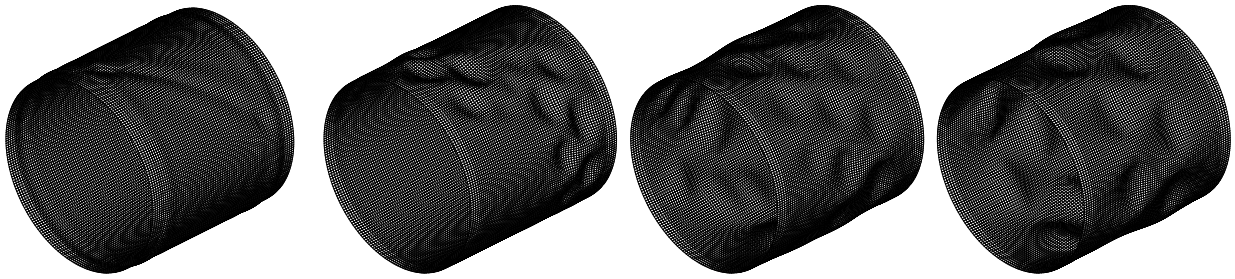

a) Prebuckling deformations
Time = 0.0 seconds
P/P_{cr} = 0.887

b) Initial collapse deformations
Time = 0.0012 seconds
P/P_{cr} = 0.885

c) Transient collapse deformations
Time = 0.0029 seconds
P/P_{cr} = 0.588

d) Post-collapse deformations
Time = 0.02 seconds
P/P_{cr} = 0.310

Fig. 17 Effects of a 45^o lamina ply-gap on the transient collapse response of a compression-loaded quasi-isotropic cylindrical shell C3.

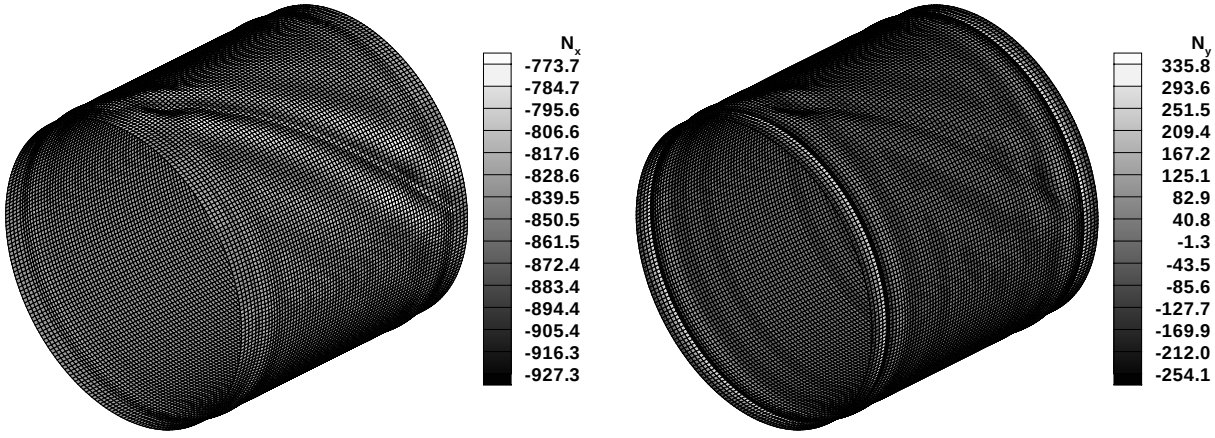

a) Axial stress resultant contours, N_x, lbf/in.

b) Circumferential stress resultant contours, N_y, lbf/in.

Fig. 18 Effects of a 45^o lamina ply-gap on the axial and circumferential stress resultants incipient to buckling for a compression-loaded quasi-isotropic cylindrical shell C3.

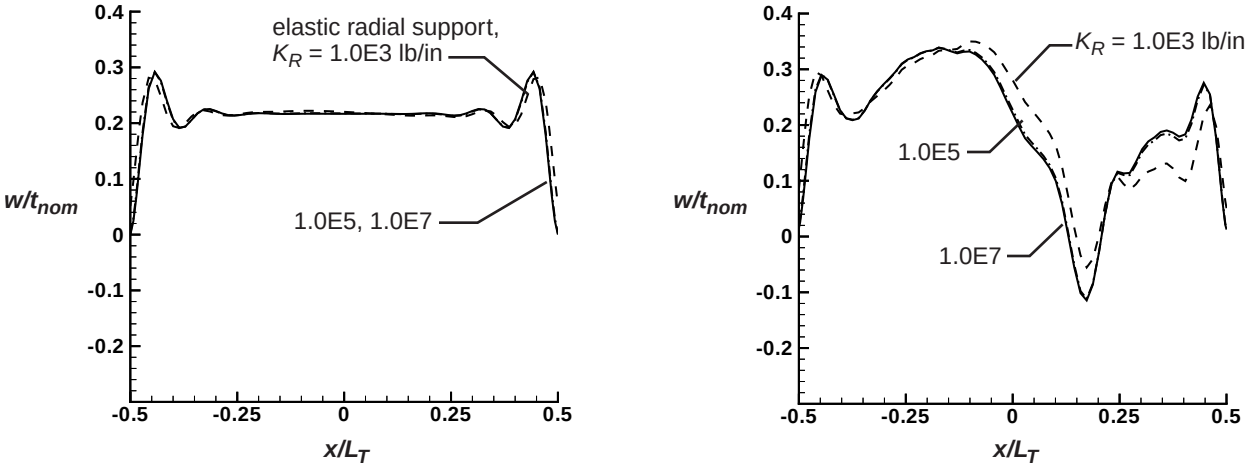

a) Geometrically perfect b) With measured imperfections

Fig. 19 Effects of elastic radial support conditions on the buckling displacement profile of compression-loaded orthotropic shell C2.

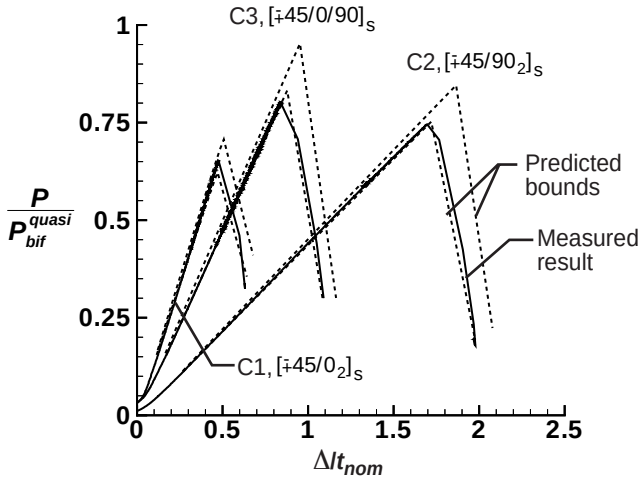

Fig. 20 Numerically predicted and experimentally measured load-shortening response curves; predicted results represent response bounds.

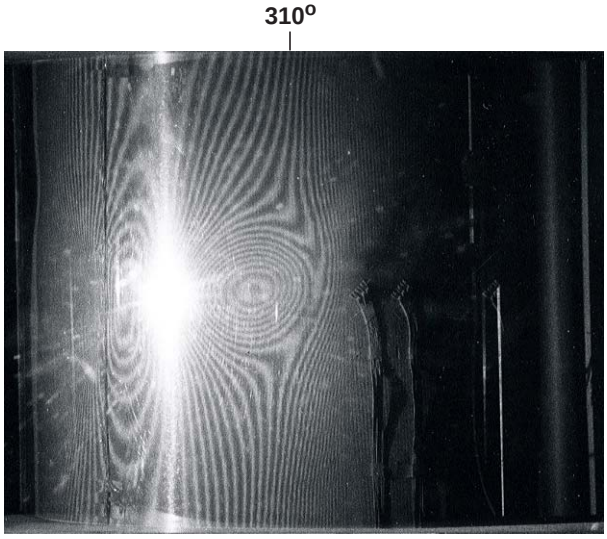

a) Observed post-collapse moiré fringe pattern.

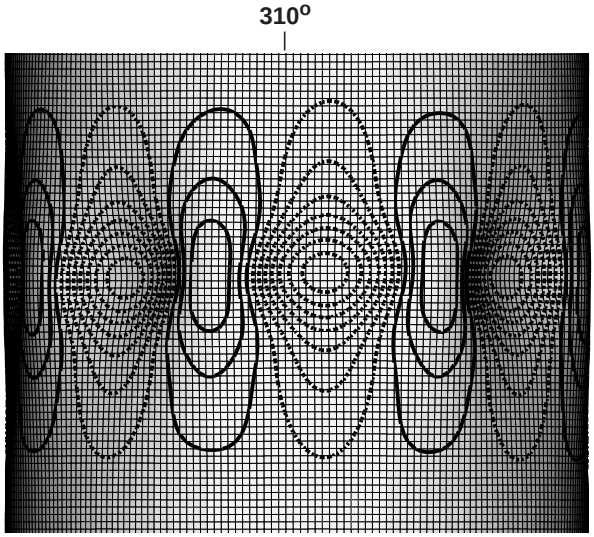

b) Numerically predicted post-collapse normal deformation response.

Fig. 21 Observed and predicted initial post-collapse normal displacements for specimen C1.

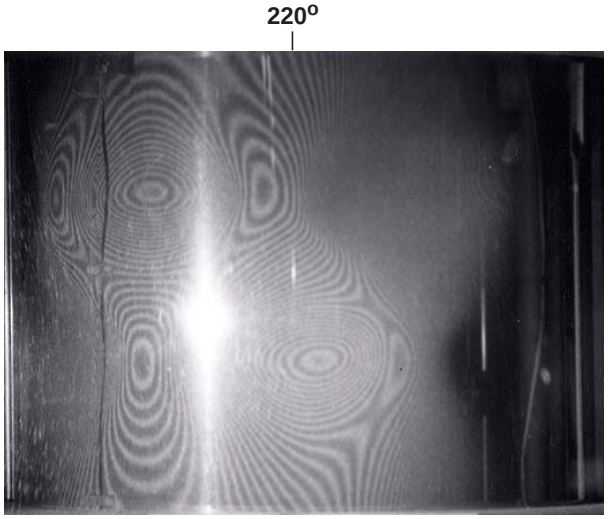

a) Observed post-collapse moiré fringe pattern.

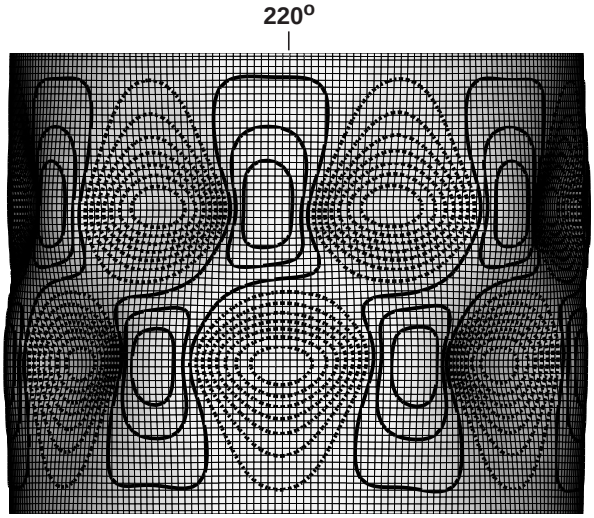

b) Numerically predicted post-collapse normal deformation response.

Fig. 22 Observed and predicted initial post-collapse normal displacements for specimen C2.

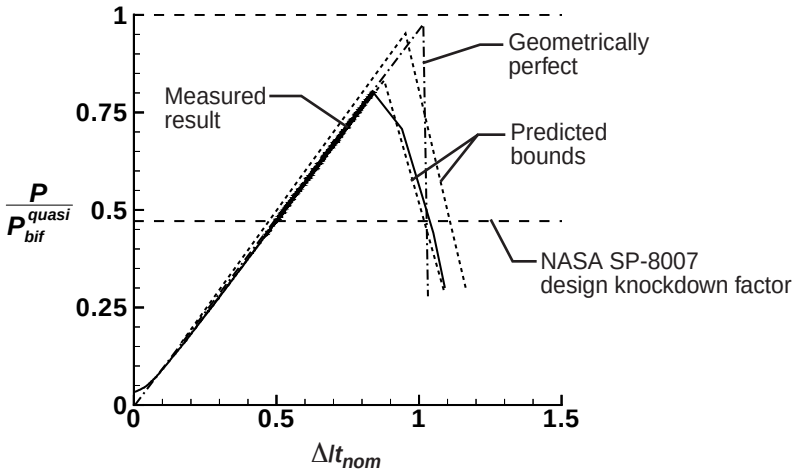

Fig. 23 Numerically predicted and experimentally measured load-strain response curves for shell C3.

REPORT DOCUMENTATION PAGE

Form Approved
OMB No. 0704-0188

The public reporting burden for this collection of information is estimated to average 1 hour per response, including the time for reviewing instructions, searching existing data sources, gathering and maintaining the data needed, and completing and reviewing the collection of information. Send comments regarding this burden estimate or any other aspect of this collection of information, including suggestions for reducing this burden, to Department of Defense, Washington Headquarters Services, Directorate for Information Operations and Reports (0704-0188), 1215 Jefferson Davis Highway, Suite 1204, Arlington, VA 22202-4302. Respondents should be aware that notwithstanding any other provision of law, no person shall be subject to any penalty for failing to comply with a collection of information if it does not display a currently valid OMB control number.
PLEASE DO NOT RETURN YOUR FORM TO THE ABOVE ADDRESS.

1. REPORT DATE *(DD-MM-YYYY)*	2. REPORT TYPE	3. DATES COVERED *(From - To)*
01- 09 - 2004	Tecnical Memorandum	

4. TITLE AND SUBTITLE

Parametric Study on the Response of Compression-Loaded Composite Shells With Geometric and Material Imperfections

5a. CONTRACT NUMBER

5b. GRANT NUMBER

5c. PROGRAM ELEMENT NUMBER

6. AUTHOR(S)

Hilburger, Mark W.; and Starnes, James H., Jr.

5d. PROJECT NUMBER

5e. TASK NUMBER

5f. WORK UNIT NUMBER

23-719-20-30

7. PERFORMING ORGANIZATION NAME(S) AND ADDRESS(ES)

NASA Langley Research Center
Hampton, VA 23681-2199

8. PERFORMING ORGANIZATION REPORT NUMBER

L-19008

9. SPONSORING/MONITORING AGENCY NAME(S) AND ADDRESS(ES)

National Aeronautics and Space Administration
Washington, DC 20546-0001

10. SPONSOR/MONITOR'S ACRONYM(S)

NASA

11. SPONSOR/MONITOR'S REPORT NUMBER(S)

NASA/TM-2004-212676

12. DISTRIBUTION/AVAILABILITY STATEMENT

Unclassified - Unlimited
Subject Category 39
Availability: NASA CASI (301) 621-0390 Distribution: Standard

13. SUPPLEMENTARY NOTES

An electronic version can be found at http://techreports.larc.nasa.gov/ltrs/ or http://ntrs.nasa.gov

14. ABSTRACT

The results of a parametric study of the effects of initial imperfections on the buckling and postbuckling response of three unstiffened thin-walled compression-loaded graphite-epoxy cylindrical shells with different orthotropic and quasi-isotropic shell-wall laminates are presented. The imperfections considered include initial geometric shell-wall mid-surface imperfections, shell-wall thickness variations, local shell-wall ply-gaps associated with the fabrication process, shell-end geometric imperfections, nonuniform applied end loads, and variations in the boundary conditions including the effects of elastic boundary conditions. A high-fidelity nonlinear shell analysis procedure that accurately accounts for the effects of these imperfections on the nonlinear responses and buckling loads of the shells is described. The analysis procedure includes a nonlinear static analysis that predicts stable response characteristics of the shells and a nonlinear transient analysis that predicts unstable response characteristics.

15. SUBJECT TERMS

Shell Buckling; Imperfections; Composites; Compression load

16. SECURITY CLASSIFICATION OF:			17. LIMITATION OF ABSTRACT	18. NUMBER OF PAGES	19a. NAME OF RESPONSIBLE PERSON
a. REPORT	b. ABSTRACT	c. THIS PAGE			STI Help Desk (email: help@sti.nasa.gov)
					19b. TELEPHONE NUMBER *(Include area code)*
U	U	U	UU	29	(301) 621-0390